ELECTROMAGNETIC PROBE AND DRIVING CIRCUIT DESIGN FOR MICRO MAGNETIC STIMULATION OF SMALL ANIMAL BRAINS

A Thesis

by

YI GUO

Submitted to the Office of Graduate and Professional Studies of
Texas A&M University
in partial fulfillment of the requirements for the degree of

MASTER OF SCIENCE

Chair of Committee,	Jun Zou
Committee Members,	"Tony" Sheng-Jen Hsieh
	Peng Li
	Pao-Tai Lin
Head of Department,	Miroslav M. Begovic

May 2019

Major Subject: Electrical Engineering

ABSTRACT

Magnetic stimulation is becoming more and more popular recently as a kind of medical treatment for brain function. By generating an alternating magnetic field from the electromagnetic probe, the induced electric field will be generated in a small region and stimulate a single or a group of neuron(s).

A functional magnetic stimulation system consists of two parts: 1) electromagnetic probe/coil, and 2) magnetic stimulation circuit. For the electromagnetic probe, several possible structures for different application were discussed. For single neuron stimulation, magnetic probe with a sharp tip was investigated. Furthermore, an optimal shape for the sharp tip was determined by analytical calculation and COMSOL Multiphysics® finite element simulation. A prototype probe was fabricated and the induced electrical field of the probe was measured combining with the magnetic stimulation circuit and an electrical field detector. For brains of some small animals like rats, a cylindrical-shaped coil was studied and the optimized shape is determined by COMSOL Multiphysics® finite element simulation.

For the magnetic stimulation circuit, a charging & control method was analyzed. Connected with a pulse generator and DC power source, the magnitude and pulse width are measured. The relationship between electronic and electromagnetic parameters was calculated and simulated with Multisim®. Furthermore, the application of an LR filter to suppress the noise was studied by calculation and simulation with Multisim®.

DEDICATION

To my family, mentors and friends

ACKNOWLEDGEMENTS

First of all, I wish to show my gratitude to my research advisor, Dr. Zou, for his earnest instruction for every step of my research work. I learned not only knowledge, but also the truth of life during the past three years. I also wish to thank my committee members Dr. Hsieh, Dr. Li, and Dr. Lin, and, for accepting to review my thesis and their consistent patience.

I would also like to thank all the colleagues of my research group. They provided me many helpful instructions in my work, which enabled me to move forward my research work more smoothly to the very end. I would also like to thank Texas A&M AggieFab and ECE staffs for their helpful guidance and assistance based on my need over my research program.

Finally, I want to show my great thankfulness to my family for their concern, love, and self-forgetful support.

CONTRIBUTORS AND FUNDING SOURCES

Contributors

This work was supervised by a thesis committee, Professor Jun Zou. All work for the thesis was completed independently by the student.

Funding Sources

There are no outside funding contributions to acknowledge related to the research and compilation of this document.

TABLE OF CONTENTS

Page

LIST OF FIGURES

Page

LIST OF TABLES

Page

CHAPTER I

INTRODUCTION AND LITERATURE REVIEW

1.1 Magnetic Stimulation

Magnetic stimulation has been used in a variety of diagnostic and therapeutic applications [1][2][3][4]. It functions by producing an alternating magnetic field, which will induce an electrical field to interact with the neurons. Compared with electrical stimulation, the main advantage of magnetic stimulation is its non-invasiveness and deep penetration capability. Current magnetic stimulation devices work by combining the electromagnetic coil and magnetic stimulation circuit. Several kinds of models have been applied to explain the mechanism of magnetic stimulation [5][6][7].

The mechanism of magnetic stimulation is related to a single nerve fiber. As shown in Figure 1.1, the direction of the electric field can be divided into two parts: parallel and perpendicular to the nerve fiber. The membrane potential can be affected by either of these two parts of the electric field. However, the perpendicular part has much less impact on the membrane potential and can be neglected.

In addition, the electric field distribution will strongly affect the stimulation outcome. For a long straight nerve fiber in a homogeneous field, the membrane potential is unaffected, and thus causes no stimulation effect. By contrast, for a long straight nerve fiber in a spatially varying field, the charge is accumulated near the membrane. The more rapid the electric field changes per length, the more the neuron will be affected. In other words, the gradient of the electric field along the nerve fiber will dominate the strength of magnetic stimulation.

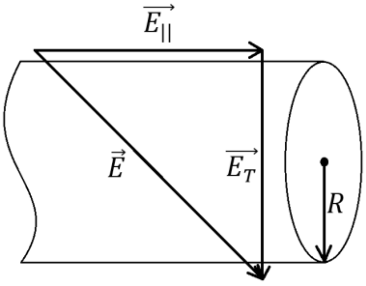

Figure 1.1 Single Nerve Fiber Model

For theories explaining the deep brain stimulation, axon cable model is useful for the definition of axonal activation, as is shown in Figure 1.2 [8]. The reaction of the axon model was simulated by acquiring several kinds of ion channel kinetics indices.

Figure 1.2 Schematic of the Axon Cable Model with the Associated Geometry Dimensions Marked in Diagram

Based on the actual stimulation mechanism, typical magnetic stimulation methods include: transcranial electrical stimulation (TES) [10], transcranial direct current stimulation (tDCS) [11], high-definition transcranial direct current stimulation (HD-tDCS) [12], transcranial alternating current stimulation (tACS) [13], transcranial random noise stimulation (tRNS) [14], cranial electrical stimulation (CES) [15], electroconvulsive therapy (ECT) [16][17], transcranial magnetic stimulation (TMS) [18], repetitive TMS (rTMS) [19], low field magnetic stimulation (LFMS) [20], and magnetic seizure therapy (MST) [17].

Before any clinical application is performed, it is a prerequisite to establish a proper understanding of the physiological processes involved in magnetic stimulations before applying magnetic stimulation techniques to any human brain. Although some methods like rTMS have been approved by the FDA (US Food and Drug Administration) [21], knowledge on its effect is still limited, and optimization methods are not so obvious. Furthermore, the FDA still considers the deep brain stimulation as a significant risk operation because the operation is some kind of invasive implant to the human body and presents a potential risk to the patients. As a result, it is necessary to apply experiments on small animals and/or single neurons to accumulate extensive data related to magnetic stimulation in ex-vivo experiments. That is why smaller scale magnetic stimulation devices are urgently needed.

Current magnetic stimulation coils are mainly designed for high current, strong magnetic flux density and deep stimulation situations. Their target application is mainly for the brains of humans and large animals. Typically, a centimeter-scale Figure-8 coil is used to generate an intense field in the junction of the coil, as is shown in Figure 1.3(a). Other configurations like circular coil are proposed, as is shown in Figure 1.3(b) [22].

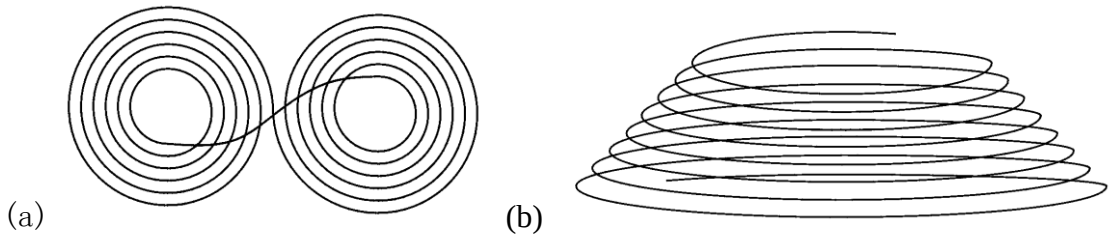

Figure 1.3 Configuration of (a) Figure-8 and (b) Circular Coil

For deep brain stimulation, implanted deep brain stimulation (DBS) electrode is commonly used, as is shown in Figure 1.4 [23]. Finite Difference Time Domain Modeling based simulation is applied to investigate the influence of geometric parameters on electric field distribution.

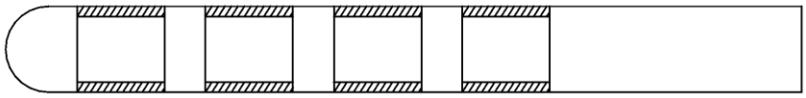

Figure 1.4 Schematic of Implanted DBS Electrode

Current magnetic stimulation coils lack the needed spatial resolution and targeting capability for localized stimulation of single or a small group of neurons. In addition, they are usually heavy and bulky, which are not suitable for wearable applications on small animal brains. What's more, for Figure-8 Coil, the active part is obscured by the coil itself, which interferes with the observation using an optic device. On the other hand, the current circular coil failed to generate an intense electric field in the center, which will be discussed in the later chapter.

1.2 Magnetic Stimulation Circuit

A Traditional circuit diagram of the electromagnetic stimulator is shown in Figure 1.5 [24]. This implementation consists of the controller, charger, gate driver, and several other electric components. Generated form LC oscillation, the shape of the pulse is usually sinusoidal. Combining charging and releasing cycle, parameters like pulse repetition frequency, train duration, and pulse width are well controlled and remain

adjustable. Other circuits like Charge-mode, Half-bridge, Full-bridge, etc. will not be discussed here since they are proposed for different applications [25][26][27].

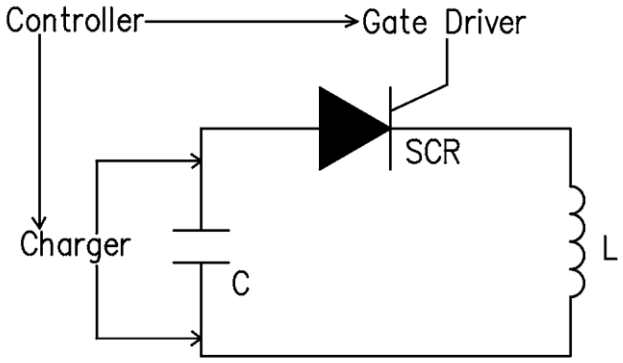

Figure 1.5 Circuit Diagram of Electromagnetic Stimulator

1.3 Magnetic Stimulation for Smaller Scale

In the past, magnetic stimulation researches for smaller scale have been investigated and developed. The dominant stimulator designs on small animals are either electrodes for tDCS or coils for TMS/μMS. For traditional electrodes used to implement tDCS, the low-current property makes it a favorable low power option. However, the required embedding operation makes the electrode method invasive and challenging.

The main coil designs for magnetic stimulation are circular and figure-8 coils, based on the recent research. The non-invasive property makes the magnetic stimulation method attractive but required high current is always a problem. Furthermore, the dominant circular and figure-8 design usually block the optical light path, which is important to the observation of the stimulation area.

1.3.1 Magnetic Stimulation on Small Animals

Magnetic stimulation in small animals is important for biomedical research because it can resemble the magnetic stimulation of human, and it requires lower costs and energy consumption [28]. Furthermore, such studies on small animals reduce the time and risk to humans [29].

Applying TMS on small animals like mice is still challenging, due to the extreme difficulty of applying high energy in a small coil. Furthermore, a large region of neural activation is not necessary [28]. Nonetheless, the coils available in the market are so large that the whole body of the small animal is usually stimulated. Therefore, small sized, light-weight stimulation coil is needed for the applications of small animals [30].

Electrodes placed on different locations are applied for electrode stimulation in a mouse model based on CT (Computed Tomography) data, as is shown in Figure 1.6 [28]. The electrodes are two round electrodes placed apart in a small distance over the stimulation region. The result of electric field distributions by finite-element simulation with COMSOL Multiphysics®. The focality increases as electrodes approach the cortical surface. Method of embedding stimulation is proved effective with a very low required current/energy but making the placement of electrodes challenging.

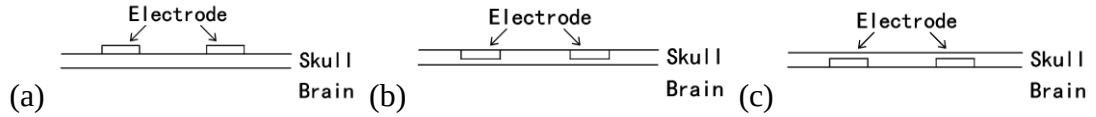

Figure 1.6 Electrode Placements for (a) Transcranial, (b) Intracranial, and (c) Cortical Surface Stimulations

A comparison of seven kinds of TMS coil configurations for the stimulation on a mouse brain is conducted, as is shown in Figure 1.7 [29]. Furthermore, conclusions on the selection of these coils according to their need are presented. The result of electric and magnetic fields is calculated by finite-element simulation with SEMCAD X. The "Slinky" and "V" coil configuration is a good choice for the stimulation of a smaller region. By contrast, the "Animal Halo" coil configuration is better for the stimulation of the entire mouse brain region. For some targeted stimulation application, the coil with the most focal electric field ("slinky") could be more advantageous than other coils.

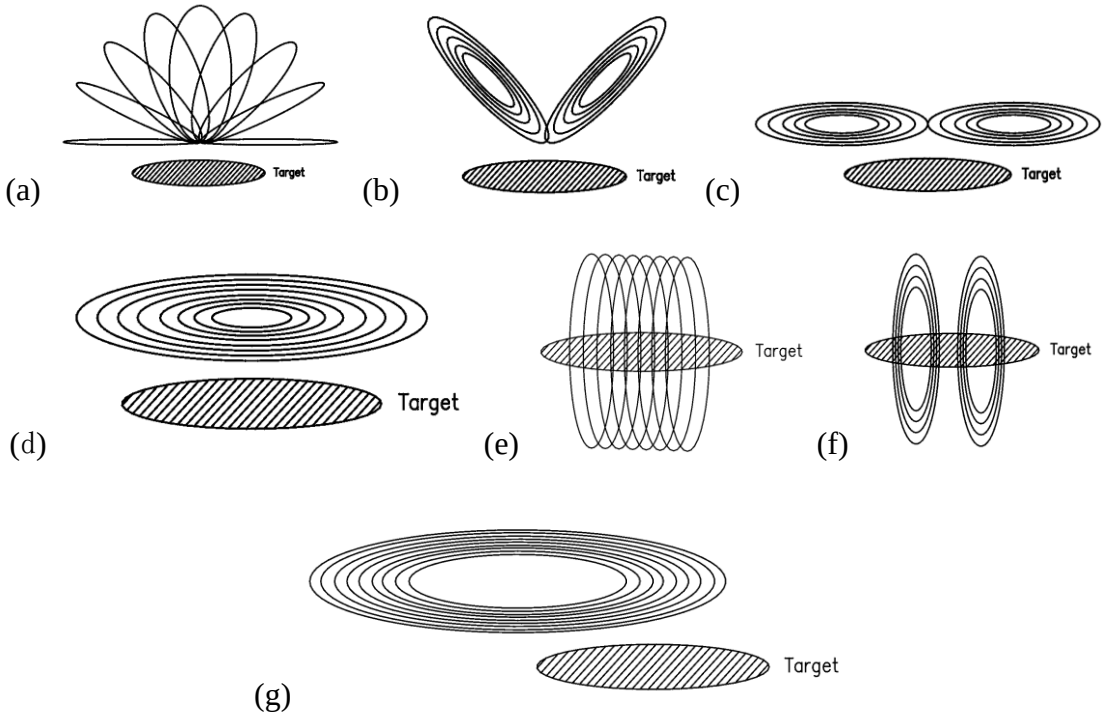

Figure 1.7 Different Coil Design: (a) "Slinky", (b) "V", (c) "Figure- Eight", (d) Circular, (e) Solenoid, (f) "Helmholtz", and (g) "Animal Halo" Shape.

A novel design of the focused coil with Sim4life modeling and measurement is conducted, as is shown in Figure 1.8 [30]. High relative permeability core is available to

be placed within the coil to enhance the magnetic flux density. With a current of 1000 A, the surface E-field can reach 93 V/m.

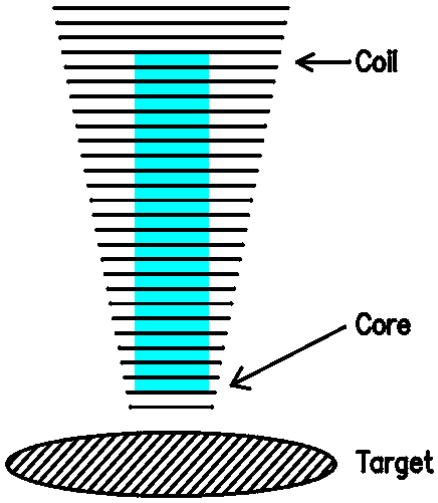

Figure 1.8 Focused Coil with Inserted Ferrimagnetic Material

The electromagnetic interference between TMS and tDCS is evaluated by applying TMS-tDCS simultaneously to an adult male Long-Evans rat. [31]. TMS was delivered with a figure-8 coil, and a pick-up coil which generates a proportional voltage to the induced electric field was positioned near the coil. In addition, a disposable electrode was placed on the scalp, and another electrode was applied to the ventral torso. Three different kinds of tDCS wiring paths are applied, as is shown in Figure 1.9. The result shows that the magnitude of TMS induced current approaches the magnitude of the tDCS current but can be reduced by shorter the electrode wiring. Finally, two practical methods for minimizing the interference during simultaneous TMS-tDCS are proposed: reducing TMS-voltage or increasing tDCS output impedance.

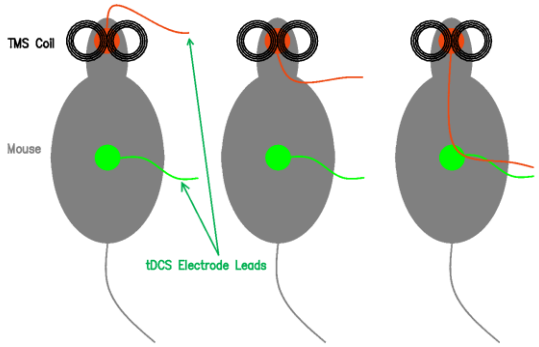

Figure 1.9 TMS-tDCS Interference Setting With Three Different Types of tDCS Electrode Wiring

The induced electric field in a mouse model by different circular and figure-8 coils in several different orientations is calculated by finite-element simulation with COMSOL Multiphysics®, as is shown in Figure 1.10 [32]. It is proposed that the secondary component will strongly counteract the main component of the electrical field. The conclusion is that the perpendicularly placed circular coils have better focality than parallel placed coils. Therefore, when conducting a magnetic stimulation with different coils, the orientation should have a higher priority than the size.

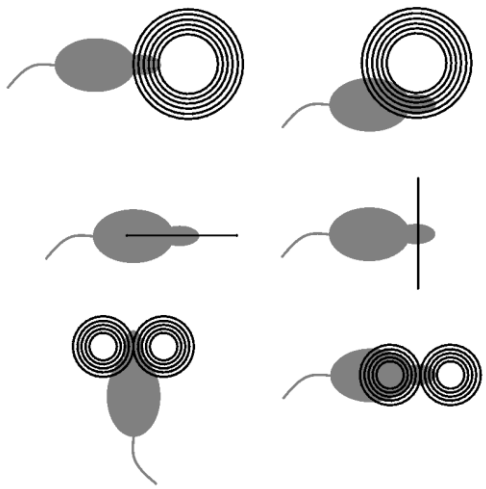

Figure 1.10 Different Coil Orientations for Circular and Figure-8 Coils

1.3.2 Magnetic Stimulation on Nerve Fibers & Neurons

The magnetic stimulation on Nerve Fibers and Neurons is named as micromagnetic stimulation (μMS). Comparing with traditional electric stimulation techniques, the inherent advantages of μMS are: targeted nerve stimulation and reduced induced heating in the tissue [33]. Furthermore, the surgical implant causing a risk of infection is not necessary for μMS. The main advantage of μMS comparing to traditional TMS is the better focality, which means targeted stimulation.

The target of μMS is aimed to stimulate multiple kinds of neurons: brain/heart neurons, retinal neurons, subthalamic nucleus neurons, pyramidal neurons, etc. The typical way of doing research on such neurons is to pick a slice sample from small animals and stimulate the sample with a tiny coil by applying multiple kinds of current waveforms.

To implement the brain and heart stimulator for neuronal stimulation, a next-generation μMS coil structure is fabricated and tested [33]. The coil is designed and optimized to maximize neural activation in specific directions and minimizing the total power consumption, and the general profile is as shown in Figure 1.11. Finally, a complete device for micromagnetic delivery was built based on thin film technology.

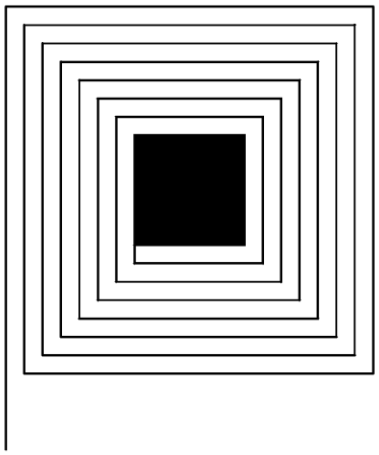

Figure 1.11 Latest Coil Design Profile

To cure retinal degenerative diseases, a non-invasive design of retinal neuron stimulation is proposed and experimentally implemented by applying two kinds of coils: Air-Core Coil and Wireless Power Charge Coil [34]. The result of field distributions is calculated by finite-element simulation with Ansoft Maxwell 3D Magnetic Ratio simulator to characterize eddy currents. Then, the duration and strength of the magnetic fields with these two kinds of coils are measured. The result shows that the wireless power charge coil yields less duration and larger strength. Finally, an in vitro experiment with retinal tissues extracted from mice is conducted.

The μMS modulation on the neural activity of the subthalamic nucleus was conducted using brain slices prepared from mice, as is shown in Figure 1.12 [35][36]. Electrophysiological experiments were conducted by applying a monophasic rectangular pulse with certain duration and several periods. The result shows that the STN (Subthalamic Nucleus) neuron response for a period and then remained deactivated for

the rest of the μMS. Therefore, the modulation strength of STN neurons is strongly related to the frequency and duration of stimulation.

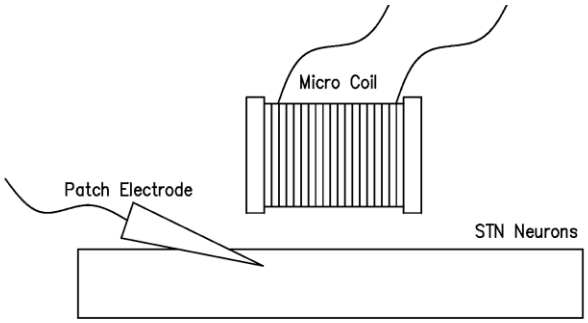

Figure 1.12 Micromagnetic Stimulation of STN Neurons

For the μMS stimulation, air-core multilayer inductors were assembled with copper wires was applied to build the μMS coil, and the input was delivered by the function generator with amplification transforming the waveform to a short-duration, high-amplitude, multi-phasic waveform. In addition, Brain slices from mice with prefrontal cortex (PFC) were used as the target of stimulation, and patch electrode was placed near the effective area to detect the response signal, as is shown in Figure 1.13 [37]. Then, waveforms were recorded and calculated with MATLAB software applications. The result shows weak activation of single pulse stimulation, but strongly modulated for certain kinds of waveforms with a certain duration delivered repetitively at 10 Hz. Furthermore, a high dependency on the direction of the coil was determined. The coil axis should be orthogonal to the targeted neuron for obvious activation.

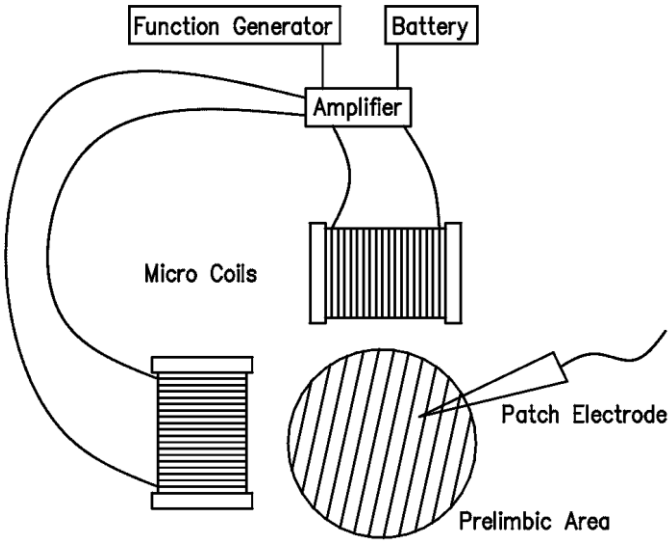

Figure 1.13 Experimental Setting of Pyramidal Neurons μMS

1.4 Requirement/Objective

The result of magnetic stimulation highly relies on the electromagnetic field profile [25]. Therefore, the effective magnetic stimulation system requires careful selection of parameters for both the stimulation circuit and the electromagnetic probe. This chapter concludes with the detailed requirements of the profile of the electromagnetic field, which highlights the objective of magnetic stimulation system design.

Based on the published literature, a typical magnetic stimulation method is designed to generate trains of bursts with breaks in between. Therefore, parameters including the shape of the pulse, interval between pulses (pulse repetition frequency), number of pulses for a train (train duration) [9], etc. are important to be determined. Another critical factor is the induced electric field intensity.

For the pulse shape, it can be either rectangular or sinusoidal. Monophasic and biphasic pulses are commonly applied [38]. Different from the monophasic pulse, the

biphasic pulse will generate an inverted current at the middle period of one burst, as is shown in Figure 1.14. Based on the literature, different current direction and pulse configuration will affect the outcome of magnetic stimulation. However, it is hard to predict the effect on a specific application.

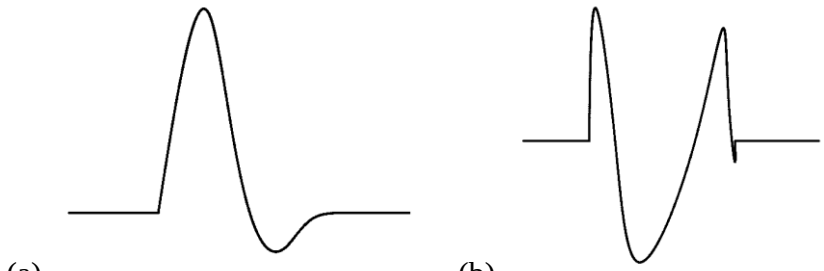

Figure 1.14 (a) Monophasic and (b) Biphasic Pulse Shape

Based on the experiment data, High frequency (5-20 Hz) excites and low frequency (< 5 Hz) inhibits the neurons [29]. A significant improvement in implicit motor learning skill occurs only at a frequency of 10 Hz [38]. For the best effect, pulse trains need to last 4 seconds with an interval of 26 seconds between pulse trains are also needed. For the amplitude of the induced electric field, an effective magnetic stimulation system should be able to induce an electric field above the neuronal activation threshold, which is 100 V/m [38].

1.5 Summary of work

This exploratory study focuses on the design and simulation of new magnetic stimulation probes and coils that are light-weight and are capable of providing focused magnetic fields for localized magnetic stimulation of small animal brains. Such

capability is important for understanding the fundamental physiological process of magnetic stimulation. In addition, a driving circuit for the magnetic stimulation probes and coils is also designed, fabricated and tested.

Chapter 2 presents the design of an electromagnetic probe and coil to improve the induced electric field. Numerical simulation is conducted to optimize the shape of the probe tip. Measurements are performed to verify the induced electric field. Various designs of the electromagnetic coil are studied and compared. A cylindrical-shaped core structure is proposed based on the results of simulation.

Chapter 3 presents the design, fabrication, and test of magnetic stimulation driving circuit. Simulation is conducted to optimize the circuit component parameters. The test results show that a desired current pulse is provided to the probe by the driving circuit. The profile of the output can be well controlled by an external pulse generator.

CHAPTER II

TMS ELECTROMAGNETIC PROBE/COIL

2.1 Electromagnetic Probe

2.1.1 Design and Analysis

The typical profile of the probe [39] is shown in Figure 2.1. The probe consists of a cylindrical body, circular truncated cone-shaped sharp tip and surrounded coil.

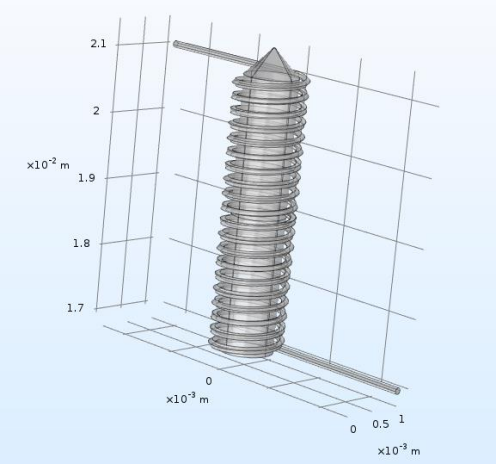

Figure 2.1 Electromagnetic Probe

Maxwell's equations governing the magnetic and electric fields, B and E, respectively, are shown in Eqs. 2.1 – 2.4.

$$\oint \vec{H} \cdot d\vec{l} = \int_S \left(\vec{J_c} + \frac{\partial \vec{D}}{\partial t}\right) \cdot d\vec{S} \tag{2.1}$$

$$\oint \vec{E} \cdot d\vec{l} = \int_S \left(-\frac{\partial \vec{B}}{\partial t}\right) \cdot d\vec{S} \tag{2.2}$$

$$\oint \vec{D} \cdot d\vec{S} = \int_V \rho \, dV \tag{2.3}$$

$$\oint \vec{B} \cdot d\vec{S} = 0 \tag{2.4}$$

Applying Eq. 2.2 to the probe, and assuming the magnetic field near the sharp tip surface are constant, one gets:

$$2\pi rE = \pi r^2 \frac{\partial B}{\partial t}, \tag{2.5}$$

where r is the radius of the circulation integral near the surface of the sharp tip. However, considering radius r could be larger than the radius of the sharp tip surface R, the relationship can be rewritten as:

$$\begin{cases} E = \frac{r}{2}\frac{\partial B}{\partial t}, & r < R \\ E = \frac{R^2}{2r}\frac{\partial B}{\partial t}, & r > R \end{cases}. \tag{2.6}$$

The relationship plot between E and r is shown in Figure 2.2:

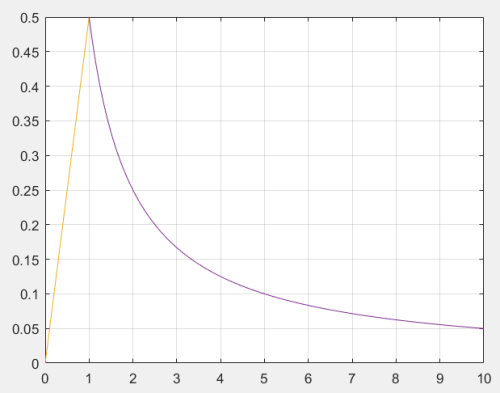

Figure 2.2 Relationship between The Induced Electric Field E and Radius r. R = 1 and ∂B/∂t = 1 are Used.

As is shown in Figure 2.2, the maximum of the induced electric field occurs when the radius of the circulation integral r equals the radius of the sharp tip surface R. The probe is assumed as a half infinity ideal solenoid with a core permeability of μ and number of windings per unit length n, the relationship between magnetic flux density B and coil current I can be determined by Equation 2.7.

$$B = \frac{1}{2}\mu nI \tag{2.7}$$

Based on the electromagnetic theory, the sharp tip confines the magnetic field in the column body and will guide it to the sharp tip of the cone, which induced much higher magnetic flux intensity on the surface of the sharp tip. A magnetic ratio (S) can be defined as the ratio between magnetic flux density inside the coil and near sharp tip surface (Equation 2.8).

$$\frac{B_{tip}}{B_{coil}} = S \ (S \geq 1) \tag{2.8}$$

Combining Equation 2.7 and 2.8, the relationship between coil current I, number of windings per unit length n, and magnetic flux density B can be determined by Equation 2.9.

$$I = \frac{2B_{coil}}{\mu_0 \mu_r n} = \frac{2B_{tip}}{\mu_0 \mu_r nS} \tag{2.9}$$

The differential version of Equation 2.9 is as Equation 2.10.

$$\left.\frac{di(t)}{dt}\right|_{max} = \frac{2}{\mu_0 \mu_r n}\left.\frac{dB_{coil}}{dt}\right|_{max} = \frac{2}{\mu_0 \mu_r nS}\left.\frac{dB_{tip}}{dt}\right|_{max} \tag{2.10}$$

Combining Equation 2.5 and 2.10, the relationship between coil current I, number of windings per unit length n, induced electric field E, Magnetic Ratio S and the radius of the sharp tip surface R can be determined by Equation 2.11.

$$E_{max} = \frac{\mu_0 \mu_r nSR}{4}\left.\frac{di(t)}{dt}\right|_{max} \tag{2.11}$$

For a given coil current, in order to maximize the induced electric field, higher permeability is needed. Higher number of windings per unit length n and slope of alternating coil current is required. What's more, the shape of the sharp tip needs to be

optimized to maximize the magnetic ratio. One thing should be noticed is that the larger the radius, the easier to generate a higher induced electric field. That's the reason why it is more difficult to generate the same induced electric field intensity in a smaller scale.

2.1.2 Core Material Selection

For the core material, higher permeability will be needed based on the previous analysis. What's more, saturation is needed to be considered. Saturation occurs when the magnetization of the material reaches a limit with the increasing external magnetic field, so the total magnetic flux density will not be able to keep the same increasing rate due to the vacuum permeability and thus the B-H curve will not remain linear for larger H, as is shown in Figure 2.3.

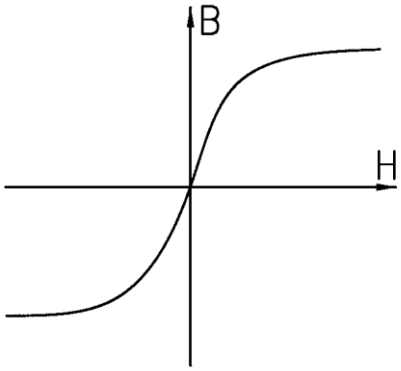

Figure 2.3 B-H Curve Caused by Saturation Effect

Taking this effect into consideration, the B-I relationship will not remain linear. No matter how current is increased, the magnetic flux density B will not be able to increase higher than saturation magnetic flux density (saturation induction), and this means a distortion for the output B of the probe, as is shown in Figure 2.3. Therefore, in order to

raise the maximum effective current limit, the material with a higher saturation induction is required.

Based on this information, the electromagnetic property of Hiperco 50/50A is considered (Table 1). Hiperco 50/50A is an alloy of 49% Cobalt and 2% vanadium, and it has a property of high magnetic saturation induction among all soft-magnetic alloys. For comparison, electromagnetic property (Saturation Induction, Permeability) of other typical materials is also listed in Table 1. Most of the materials do not have the property suits for the implementation, because they do not have a high relative permeability and saturation `induction at the same time. Cobalt-iron can be another option.

Medium	Relative Permeability (to air)	Saturation Induction (T)
Metglas 2714A	1000000	0.57
Mu-metal	20000	0.8
Cobalt-iron	18000	2.2
Hiperco 50A	15000	2.4
Hiperco 50	12000	2.4
Permalloy	8000	1

Table 1 Electromagnetic Property of Typical Materials

2.1.3 Simulation

The main steps of COMSOL Multiphysics® setting consist of 4 parts: Geometry, Materials, Magnetic and Electric Fields and Study. The detailed parameters are shown in Table 2.

Geometry			
Component	Geometry	parameter	value
core	cylindar	radius (mm)	0.4
		height (mm)	4
	cone	bottom radius (mm)	0.4
		height (mm)	0.8 - 1.3
		top radius (mm)	0.02
coil	helix	number of turns	20
		major radius (mm)	0.5
		minor radius (mm)	0.05
		axial pitch (mm)	0.2

Materials			
Name	Property Value		
	relative permeability	relative permittivity	electrical conductivity (S/m)
air	1	1	1
nickel steel supermalloy	15000	1	1.74M
copper	1	1	60M

Others	
Coil current (A)	10
Frequency (Hz)	100K

Table 2 Parameters of COMSOL Multiphysics Settings for Electromagnetic Probe

For Geometry, the radius of the core is 0.4 mm and the radius of the coil is 0.5 mm. The height of the core is adjustable for a different number of turns of the coil, and the number of turns per length is fixed. To build up this structure, Primitive Geometries (cylinder, cone, extrude, etc.), Booleans (union, difference, etc.) and Partitions are applied.

For Materials, the main materials are air, nickel steel Supermalloy (Hiperco 50) and copper. The main properties are relative permeability, relative permittivity and electrical conductivity.

For Magnetic and Electric Fields, the critical setting is mainly for coils. The coil is set to numeric type and the coil current is set to 10A.

For comparison, parametric sweep and frequency domain settings are needed. Parametric sweep is useful for doing a bunch of simulation with one or several changing parameters and the setting of the frequency domain is mainly for setting the frequency. For this simulation, the parameter sweep from 0.8 - 1.3 mm on the height of the tip is applied, and the frequency is set to 100 kHz.

The result of Magnetic flux density with 1.3mm tip height obtained by finite-element simulation with COMSOL Multiphysics® is as is shown in Figure 2.4(a). As is shown in Figure 2.4(b), a strong magnetic flux density is generated near the sharp tip of the core, which is around 1.5 Tesla. Comparing with the result that the magnetic flux density near the surface without a core in the same condition is around 0.2 Tesla, the magnetic ratio S can be calculated as Equation 2.12 based on Equation 2.8.

$$S = \frac{B_{tip}}{B_{coil}} = \frac{1.5T}{0.2T} = 7.5 \tag{2.12}$$

With a driving current of 10 Amp, the coil generated an electric field of 20 V/m. Therefore, around 50 Amp current is needed to generate a 100 V/m induced electric field. The result of the induced electric field obtained by finite-element simulation with COMSOL Multiphysics® is as is shown in Figure 2.5.

(a) 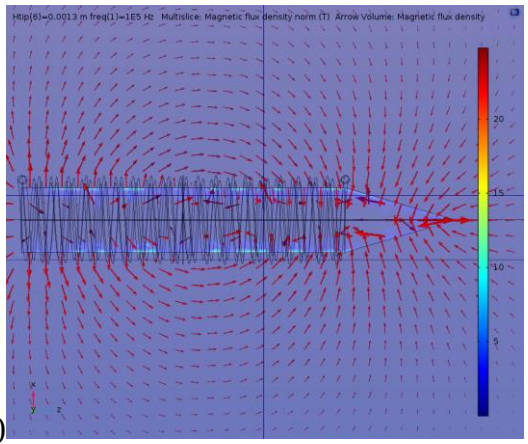 (b) 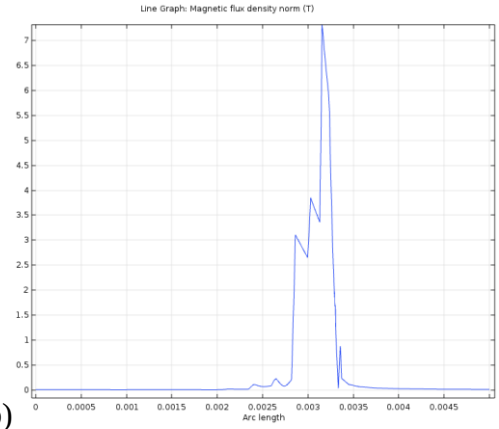

Figure 2.4 Magnetic Flux Density: (a) Arrow Volume and (b) Along Axis with 1.3mm Tip Height

(a) 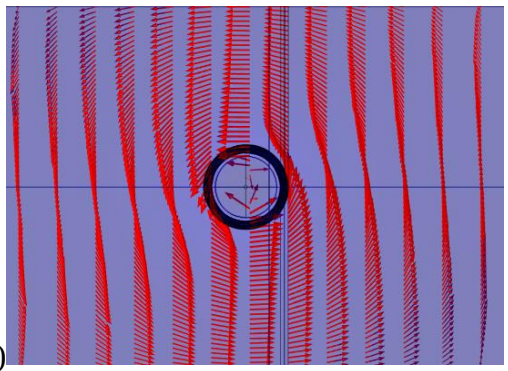 (b) 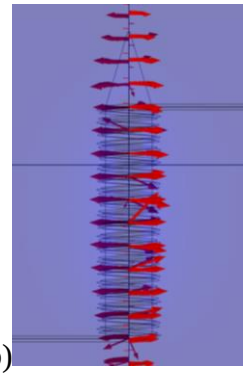

Figure 2.5 (a) Upper and (b) Side View of Induced Electric Field

There is a stronger induced electric field generated near the side of the core than the tip. In this simulation, the intensity generated near the side of the core is around 140 V/m with the same driving current of 10 Amp, which is 7 times larger than near the tip. Therefore, the side of the core can be selected for a regular application requiring higher electric field intensity stimulation, and the sharp tip is a better selection for finer, limited region, and lower intensity cases. Another parameter is the length of the sharp tip. For a different length of the tip, the performance is different. Therefore, parameter sweep is

performed with COMSOL Multiphysics®, as is shown in Figure 2.6. The length of the tip is from 0.8 mm to 1.3 mm. From Figure 2.6, The maximum electric field is induced when the height of the tip is around 1.2 mm for 0.4 mm bottom radius cone. Therefore, 1.2 mm is the best tip height for a core with 0.4 mm radius.

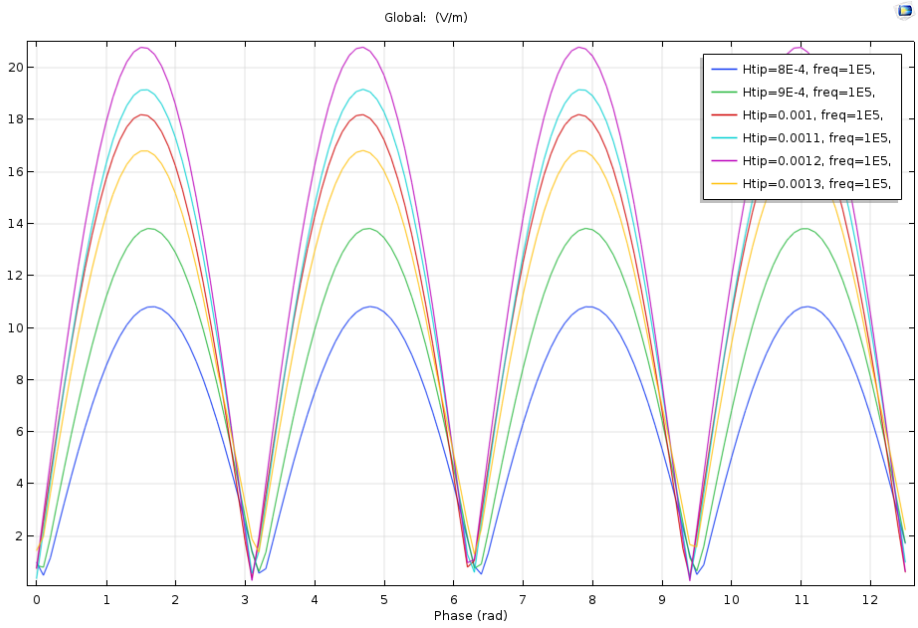

Figure 2.6 Induced Electric Field for Different Tip Height from 0.8 mm to 1.3 mm

2.1.4 Implementation

A prototype needle probe and the induced electric field detection circuit is constructed (Figure 2.7). For the needle, it is composed of 1 × 0.36 × 20 mm cubic Hiperco50 core winded with AWG38 copper coil for 50 turns. The additional copper wire is wined for 5 turns on the side of the coil and the voltage of this detection coil equals the integration of induced electric field on the side of the coil. Now that side of the coil is being used, assuming R as R_{core} and S equal to 1, the induced electric field follow the Equation 2.13 based on Equation 2.11.

$$E_{max} = \frac{\mu_0 \mu_r nR}{4} \frac{di(t)}{dt}\Big|_{max} \quad (2.13)$$

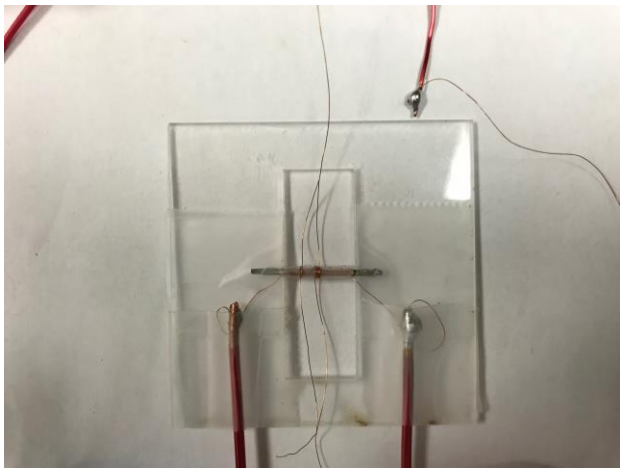

Figure 2.7 A Prototype Needle Probe and the Induced Electric Field Detection Coil

Therefore, to reach the 100 V/m induced electric field requirement, a sharper current pulse is required. If the voltage of the detection coil is acquired, and the number of turns and the parameters of the probe are known, the induced electric field can be estimated by Equation 2.14.

$$E = \frac{U}{l} = \frac{U}{2n(a+b)} \quad (2.14)$$

For this implementation, to reach the induced electric field of 100 V/m, the required voltage can be calculated as Equation 2.15.

$$U = 2n(a+b)E = 2 \times 5 \times (1 + 0.36) \times 100m = 1.36V \quad (2.15)$$

2.1.5 Conclusion

The design of the electromagnetic probe is estimated to generate the 100 V/m induced electric field on the tip with a 50 Amp current pulse in the coil. What's more, if

the side of the core than the tip is being used, about 7 times stronger induced electric field can be generated, which means that only 7 Amp current pulse is needed for 100 V/m induced electric field application.

A prototype needle probe and an induced electric field detection coil are designed and implemented to verify the simulation result. It is calculated that a 1.36V voltage is required to reach the induced electric field of 100 V/m near the side of the probe.

2.2 Electromagnetic Coil

The experiment on the probe is successful. However, it is not available for generating a large area of an intense electric field. The figure-8 coil is the most common case, but it is not convenient for optical equipment to directly observe the stimulation area. Therefore, a hollow cylindrical-shaped core structure is proposed, and several kinds of configurations are compared.

2.2.1 Design, Analysis & Simulation

The optimized shape is the truncated-cone-shaped structure because it is very suitable to put on a mouse head. The profile and current direction are as shown in Figure 2.8. The coil structure is formed by revolving a rectangular shape. The detailed parameters for COMSOL Multiphysics® simulation are shown in Table 3.

Geometry			
Component	Geometry	parameter	value
coil	Rectangular(2D)	width (mm)	4
		height (mm)	46
		rotation(degree)	26.565
		revolve	Y axis, distance center: 28mm
		number of turns	50
Others			
Coil current (A)		10	
Frequency (Hz)		100K	

Table 3 Parameters of COMSOL Multiphysics Settings for Truncated-Cone-Shaped Electromagnetic Coil

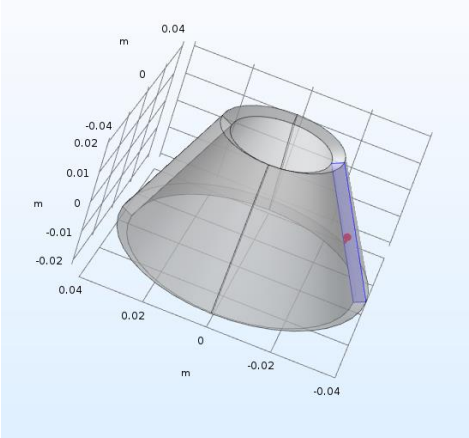

Figure 2.8 Truncated-Cone-Shaped Electromagnetic Coil

The result of Magnetic flux density obtained by finite-element simulation with COMSOL Multiphysics® is as is shown in Figure 2.9. From Figure 2.9, a strong magnetic field is generated in the inner space of the coil. However, based on the simulation result of the induced electric as shown in Figure 2.10, such a structure fails to generate an effective electric field in the center region where the mouse brain lies in.

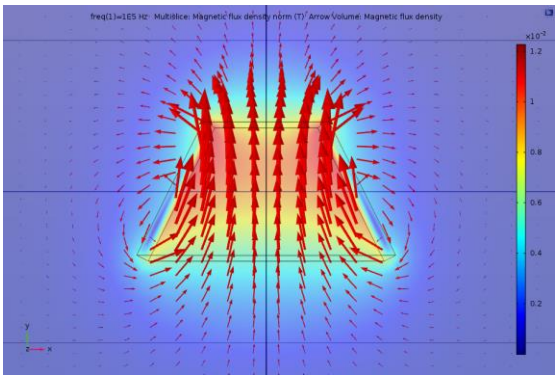

Figure 2.9 Magnetic Flux Density of Truncated-Cone Structure

(a) 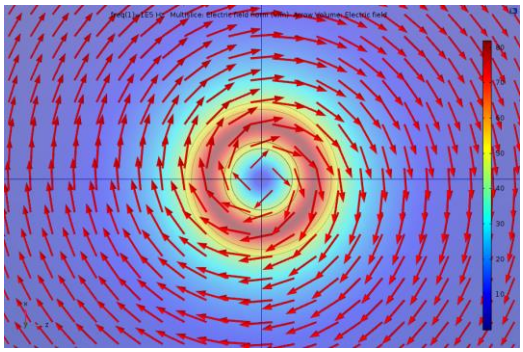 (b) 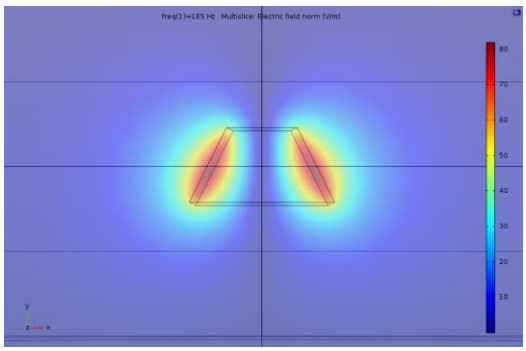

Figure 2.10 (a) Upper and (b) Side View of Truncated-Cone Induced Electric Field

To fix this problem, different current direction for the same configuration is attempted. The profile and current direction are as shown in Figure 2.11(a). The structure is formed by revolving a work plane geometry, as is shown in Figure 2.11(b). The detailed parameters for COMSOL Multiphysics® simulation are shown in Table 4.

Geometry			
Component	Geometry	parameter	value
coil	Shape (2D)	outer radius (mm)	10
		Inner radius (mm)	6
		circle center distance (mm)	46
		rotation (degree)	26.565
		revolve	Y axis, distance center: 28mm
		number of turns	50
Others			
Coil current (A)		10	
Frequency (Hz)		100K	

Table 4 Parameters of COMSOL Multiphysics Settings for Another Truncated-Cone-Shaped Electromagnetic Coil

(a) 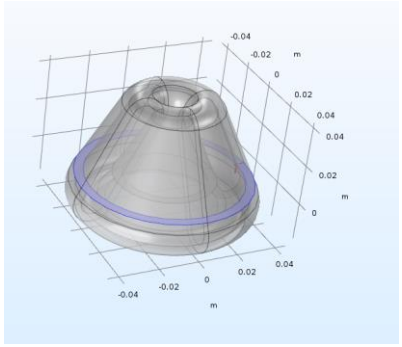 (b) 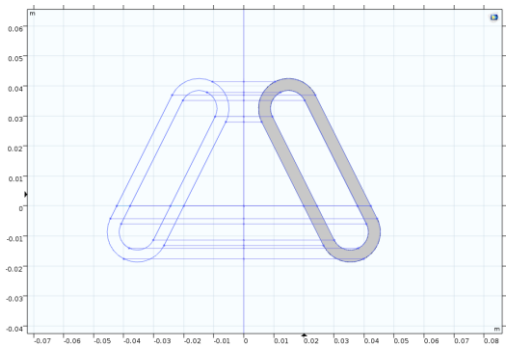

Figure 2.11 Another Truncated-Cone-Shaped Electromagnetic Coil (a) 3D (b) Plane Geometry

The result of Magnetic flux density obtained by finite-element simulation with COMSOL Multiphysics® is as is shown in Figure 2.12. The interesting part is that the generated magnetic field is mainly confined inside the coil. Therefore, the interference of the magnetic field is minimized when compared with the first one.

(a) 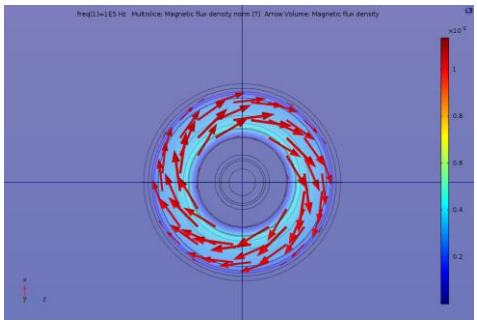 (b) 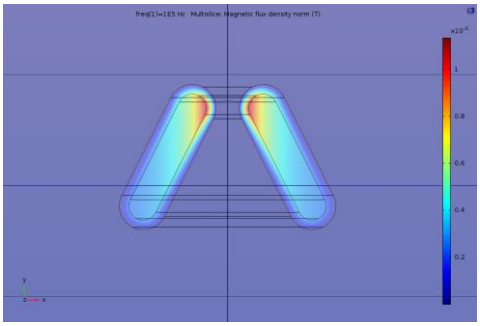

Figure 2.12 (a) Upper and (b) Side View of Magnetic Flux Density of Modified Truncated-Cone Structure

The simulation result of the induced electric is shown in Figure 2.13. A strong electric field is generated near the top of the structure. However, a less strong electric field is generated in the center of the structure. Therefore, such structure is also not so effective to generate a strong electric field in the center region where the mouse brain lies in. Nevertheless, a higher electric field is observed in the effective region.

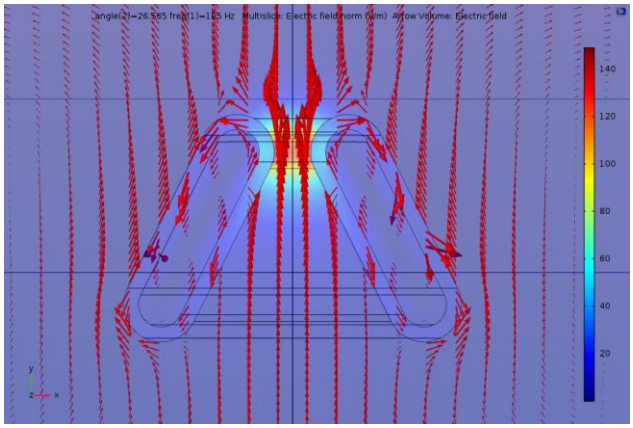

Figure 2.13 Induced Electric Field of Modified Truncated-Cone Structure

To generate an effective even distributed field in the inner region, another cylindrical structure is attempted. The cylindrical structure is simply derived by

changing the rotation angle in Table 4 to 0 degree. The profile and current direction are as shown in Figure 2.14.

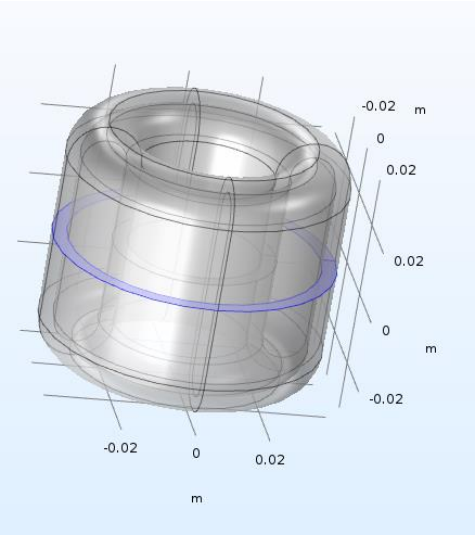

Figure 2.14 Cylindrical-Shaped Electromagnetic Coil

The simulation result of the magnetic flux density and the induced electric field obtained by finite-element simulation with COMSOL Multiphysics® is as shown in Figure 2.15.

(a) 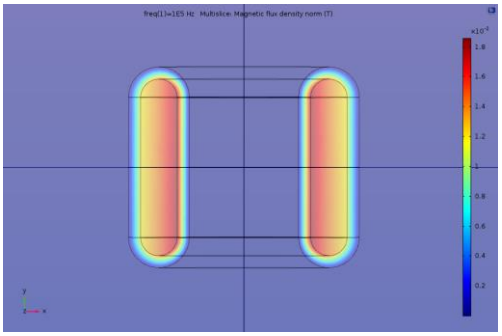 (b) 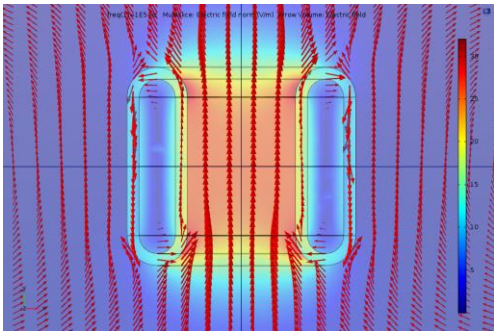

Figure 2.15 (a) Magnetic Flux Density and (b) Induced Electric field of Cylindrical Structure

For the cylindrical-shaped structure, the distributing magnetic field is also well confined inside the coil. With a driving current of 10 Amp, the coil generates an evenly distributed electric field of 30 V/m in the inner region. Therefore, 33 Amp current is required for 100 V/m induced electric field. For higher electric field application, a cylindrical-annulus-shaped core can be added to this structure to enhance the intensity of the electric field further. For the Hiperco 50A with a relative permeability of 15000, the induced electrical field can be 15000 times higher, which means only 0.002 Amp current is needed. However, the property of saturation induction will affect the induced electrical field in practice.

2.2.2 Weight & Heat Consideration

Considering that it is designed for use on the mouse head, weight and heat dissipation consideration are critical for making this design practical. For the cylindrical coil design, assume that the radius of the copper wire and height of the cylindrical-shaped structure to be r_w and h, and the number of turns to be N_t. The space between wires is neglected compared to the radius and height. The mass of the electromagnetic coil can be calculated as

$$m = 2\rho_{copper}\pi {r_w}^2 h N_t \tag{2.16}$$

The resistance of the coil can be calculated as

$$R = \rho\frac{l}{s} = \frac{2\rho_{copper} h N_t}{\pi {r_w}^2} \tag{2.17}$$

Therefore, the power consumption can be calculated as

$$P = I^2R = \frac{2I^2\rho_{copper}hN_t}{\pi {r_w}^2} \quad (2.18)$$

Based on Equation 2.16 - 2.18, in order to generate a larger region of the electrical field, h and N_t will increase, which in turn increases the weight and heat dissipation. Applying thicker wire for the coil will benefit power consumption, but it will also make the weight heavier. Increasing current will benefit the intensity of the induced electric field, but also higher the power dissipation. If an additional core is applied for this design, the intensity of the induced electric field will be significantly higher, but the mass and heat dissipation will be dramatically increased.

2.2.3 Conclusion

The final design is a cylindrical-shaped electromagnetic coil with the proper current direction. Without a core, it is estimated to generate the required 100 V/m induced electric field on the tip with a 33 Amp current pulse in the coil. A high-permeability cylindrical-annulus-shaped core can be added to enhance the electric field further or lower the required current. Other designs are not considered because of the unavailability of generating a strong electric field in the proper region. A trade-off is found between weigh, heat, induced electric field, and size for this coil design.

CHAPTER III

MAGNETIC STIMULATION CIRCUIT

3.1 Design and Analysis

As is illustrated in the previous chapters, the traditional topology of the electromagnetic stimulator is shown in Figure 1.5. Adapting from this topology, the schematic of the design is shown in Figure 3.1 [40]. The gate is driven and controlled by a function generator V_2, and direct current voltage source V_1, Resistor R_1, and Inductor L_1 consist the charger part for capacitor C_1. In addition, the probe is regarded as an inductor L_2.

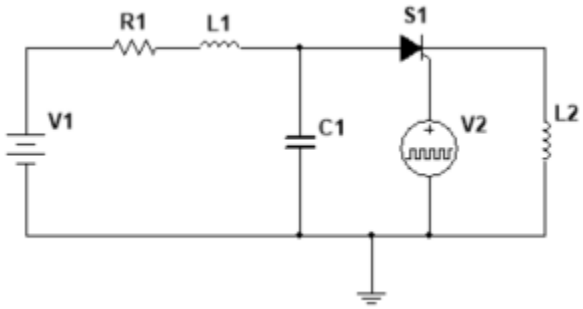

Figure 3.1 Prototype Schematic of Magnetic Stimulation Circuit

3.1.1 Charging Cycle

For charging cycle, SCR S_1 is shut down, so the functional components will only be Charger including V_1, R_1, L_1, and capacitor C_1. If $L_1 = 0$, based on the basic circuit theory, the voltage of V_C can be derived as

$$V_C(t) = V_1(1 - e^{-\frac{t}{C_1 R_1}}) \tag{3.1}$$

The peak current will be $\frac{V_1}{R_1}$ when t = 0.

For higher R_1, the amplitude of the peak current can be lower, which is beneficial for circuit protection. However, higher R_1 or C_1 will also longer the charging time, making the circuit not suit for high-frequency stimulation situation.

If $L_1 \neq 0$ and $R_1^2 C_1 > 4L_1$, based on the basic circuit theory, Equation 3.2 can be derived.

$$\begin{cases} \dfrac{dI}{dt} = \dfrac{U_{L1}}{L_1} \\ I = C_1 \dfrac{dU_{C1}}{dt} = \dfrac{U_{R1}}{R_1} \\ V_1 = U_{L1} + U_{R1} + U_{C1} \end{cases} \tag{3.2}$$

Combining with the facts of Equation 3.3.

$$\begin{cases} U_{C1}|_0 = 0 \\ I = I_{L1}|_0 = 0 \end{cases} \tag{3.3}$$

V_C and I follow the relationship of Equation 3.4 – 3.5:

$$V_C(t) = V_1\left(1 + \frac{2L_1}{C_1 {R_1}^2 - 4L_1 - C_1 R_1 \sqrt{{R_1}^2 - 4\frac{L_1}{C_1}}} e^{\frac{-R_1 + \sqrt{{R_1}^2 - 4\frac{L_1}{C_1}}}{2L_1} t} + \frac{2L_1}{C_1 {R_1}^2 - 4L_1 + C_1 R_1 \sqrt{{R_1}^2 - 4\frac{L_1}{C_1}}} e^{-\frac{R_1 + \sqrt{{R_1}^2 - 4\frac{L_1}{C_1}}}{2L_1} t}\right) \tag{3.4}$$

$$I(t) = \frac{V_1}{\sqrt{{R_1}^2 - 4\frac{L_1}{C_1}}} e^{-\frac{R_1}{2L_1} t}\left(e^{\frac{\sqrt{{R_1}^2 - 4\frac{L_1}{C_1}}}{2L_1} t} - e^{-\frac{\sqrt{{R_1}^2 - 4\frac{L_1}{C_1}}}{2L_1} t}\right) = \frac{2V_1}{\sqrt{{R_1}^2 - 4\frac{L_1}{C_1}}} e^{-\frac{R_1}{2L_1} t} sh\left(\frac{\sqrt{{R_1}^2 - 4\frac{L_1}{C}}}{2L_1} t\right) \tag{3.5}$$

If parameter V_1=2V, R_1=100Ω, L_1=50mH, C_1=20μF, the relationship between I and t is shown in Figure 3.2.

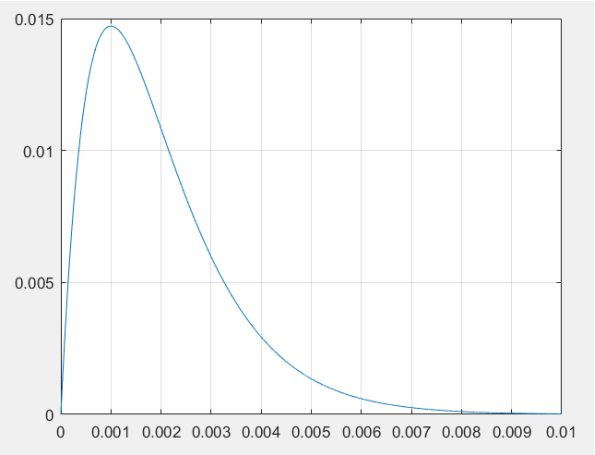

Figure 3.2 I-t Relationship When $L_1 \neq 0$ and $R_1^2C_1 > 4L_1$

Comparing with the $L_1 = 0$ situation, if a proper value for L_1 is chosen, this circuit can be optimized by making the charging cycle faster and preventing the circuit from suffering a huge current.

However, if $L_1 \neq 0$ and $R_1^2C_1 < 4L_1$, based on the Equation 3.2 - 3.3, the derived V_C and I will follow Equations 3.6 – 3.7.

$$V_C = V_1 - \frac{V_1}{\sqrt{4\frac{L_1}{C_1} - {R_1}^2}} e^{-\frac{R_1}{2L_1}t}\left[R_1 \sin\left(\frac{\sqrt{4\frac{L_1}{C_1} - {R_1}^2}}{2L_1}t\right) + \sqrt{4\frac{L_1}{C_1} - {R_1}^2}\cos\left(\frac{\sqrt{4\frac{L_1}{C_1} - {R_1}^2}}{2L_1}t\right)\right] \tag{3.6}$$

$$I = \frac{2V_1}{\sqrt{4\frac{L_1}{C_1} - {R_1}^2}} e^{-\frac{R_1}{2L_1}t} \sin\left(\frac{\sqrt{4\frac{L_1}{C_1} - {R_1}^2}}{2L_1}t\right) \tag{3.7}$$

For V_1=2V, R_1=100Ω, L_1=1H, C_1=20μF, the relationship between I and t is shown in Figure 3.3. If the value of L_1 is not appropriate, the voltage will suffer a fluctuation and it will take much more time to be stable, which should be avoided.

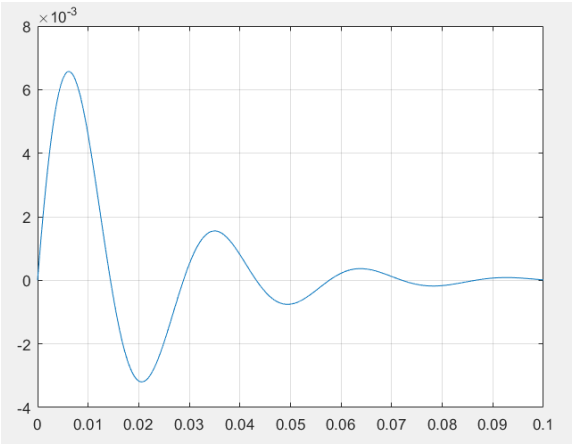

Figure 3.3 I-t Relationship When $L_1 \neq 0$ and $R_1^2C_1 > 4L_1$

3.1.2 Releasing Cycle

For releasing cycle, SCR S_1 is switched on, so the charger and capacitor will be connected to the probe L_2.

During the releasing cycle, capacitor C_1 will be affected by both charger and probe. However, in order to design a functional circuit, charging time will be set in an order of milliseconds whereas the pulse width of the releasing current will be in an order of microseconds. Therefore, the influence from the charger could be neglected. Based on this situation, the functional components will only be capacitor C_1 and probe L_2, with a certain amount of parasitic resistance.

When parasitic resistance is neglected, the releasing circuit can be regarded as a typical LC oscillation circuit. Therefore, the derived V_{probe} and I_{probe} can be expressed as

$$V_{probe} = V_1 \cos \frac{t}{\sqrt{L_2 C_1}} \tag{3.8}$$

$$I_{probe} = V_1 \sqrt{\frac{C_1}{L_2}} \sin \frac{t}{\sqrt{L_2 C_1}} \tag{3.9}$$

As a result, the parameters of resulted current pulse including amplitude and pulse width can be well controlled by the parameters of electronics components including the voltage of DC source V_1, Inductance of the probe L_2 and the capacitance C_1. Higher V_1, C_1 or lower L_2 will increase the amplitude of the current pulse, and higher C_1 or L_2 will higher the width of the pulse.

3.1.3 Improvement: LR Filter

For this implementation, the occurrence of high-frequency glitch can affect the overall performance of the system. To reduce the noise, the low pass filter is useful for this situation. The expected effect is to get rid of the high-frequency glitch as well as minimize the negative effect on the low-frequency current pulse.

The most commonly used filter is the RC filter shown in Figure 3.4(a). However, it is not applicable to this implementation. The reason is that the capacitor in parallel with the probe will form an LC resonator. Therefore, the solution is to apply an LR filter, as is shown in Figure 3.4(b).

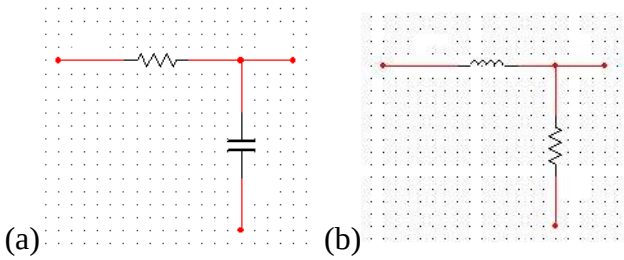

Figure 3.4 (a) RC and (b) LR Filter

For an LR filter, the network function is

$$H(s) = \frac{R}{R+j\omega L} \tag{3.10}$$

To make the LR filter effective for this implementation, 3dB bandwidth should between the signal and noise frequency, as is shown in Equation 3.11.

$$f_{signal} < f_{3dB} = \frac{R}{2\pi L} < f_{noise} \tag{3.11}$$

For the releasing cycle part, the schematic is as shown in Figure 3.5. To determine the value of Z_1, Z_2, and Z_3, the current can be calculated as.

$$I = \frac{\frac{Z_2 Z_3}{Z_2+Z_3}}{(Z_1+\frac{Z_2 Z_3}{Z_2+Z_3})Z_3} = \frac{Z_2}{Z_1 Z_2+Z_2 Z_3+Z_1 Z_3} \tag{3.12}$$

With impedance of these components applied, the current and the magnitude of the current is expressed as

$$I = \frac{1}{j\omega(L_{filter}+L_{probe})-\omega^2 L_{filter}L_{probe}/R} \tag{3.13}$$

$$|I_3| = \frac{1}{\omega\sqrt{(L_{filter}+L_{probe})^2+(\omega L_{filter}L_{probe}/R)^2}} \tag{3.14}$$

To effectively filter the high frequency noise and retain the low frequency current pulse, Equation 3.15 should be satisfied near the coil current signal frequency.

$$Z_{filter\_inductor} \ll Z_{probe} \ll R \tag{3.15}$$

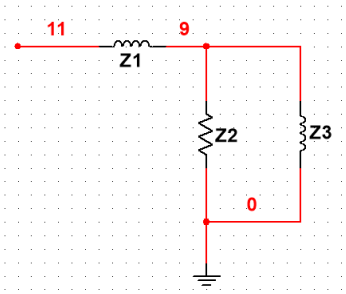

Figure 3.5 Circuit Diagram of Releasing Cycle Part

3.2 Implementation

3.2.1 Parameter Selection & Simulation

Based on Equation 3.9 and requirements discussed in previous chapters, the pulse width should be within 2.5μs, the relationship between L_2 and C_1 should follow Equation 3.16 – 3.17.

$$t_{pulse} = \pi\sqrt{L_2 C_1} = 2.5\mu s \tag{3.16}$$

$$\sqrt{L_2 C_1} = \frac{t_{pulse}}{\pi} = 0.80\mu s \tag{3.17}$$

To acquire the inductance of the electromagnetic probe, an LCR Meter is used. For inductance, it has two models: serial and parallel model, as is shown in Figure 3.6.

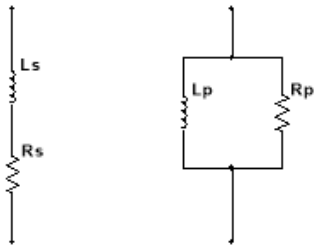

Figure 3.6 Serial & Parallel Models for LCR Meter for Inductance Measurement

Using LCR meter, the test result of the electromagnetic probe is as Table 5.

Frequency (Hz)	100	120	1K	10K	20K	100K
Ls/Lp (F)	30μ/100m	30μ/3m	15μ/57m	12μ/16u	11μ/11μ	10μ/11μ

Table 5 Test Result of LCR Meter

For this implementation, the frequency is around 100K and serial model should be applied, so the L_2 is 10μF. Therefore, the capacitance can be calculated from Equation 3.18 based on Equation 3.16 – 3.17.

$$C_1 = \frac{{t_{pulse}}^2}{\pi^2 L_2} = \frac{(0.80\times10^{-6})^2}{1\times10^{-5}} = 6.4\times10^{-8}F \approx 64nF \tag{3.18}$$

To reach an induced electric field of 100 V/m, the magnitude of the current pulse should be at least 7A. Combining with the result of simulation and Equation 3.9, the least voltage for V_1 is determined as

$$V_1 = I_{max}\sqrt{\frac{L_2}{C_1}} = 7\times\sqrt{\frac{10\mu}{64n}} = 87.5V \tag{3.19}$$

For the implementation of the charging cycle, L_1 is set to 0. To protect the circuit, a larger value of R_1 should be chosen to avoid huge current burning the circuit. However, based on Equation 3.1, the higher the R_1, the longer the charging cycle. The time constant τ of the charging cycle should be much faster than the period of bursts, which is around 10 Hz. Therefore, the value of R_1 should be determined by

$$\frac{V_1}{I_{charge\_max}} < R_1 \ll \frac{1}{f_{burst}C_1} \tag{3.20}$$

Another consideration for R_1 is SCR. The peak current should never exceed the breakdown current of the SCR. Otherwise, the charging cycle will break down, and the

magnitude of the current pulse will be limited. Therefore, R_1 should be high enough to acquire a higher current pulse in the coil of the probe.

The V_2 is a pulse generator, which should be able to generate a pulse train of 10 Hz. The duty ratio can be calculated by Equation 3.21.

$$Duty\ Ratio = \frac{t_{pulse}}{T_{burst}} = 5\mu s \times 10Hz = 5 \times 10^{-5} = 0.005\% \qquad (3.21)$$

In order to verify the calculation, simulation with Multisim® is performed, the schematic and simulation result is shown in Figure 3.7 - 3.8. the magnitude of the current is 28.2A and the pulse width is 2.52μs, which corresponds to the calculation results.

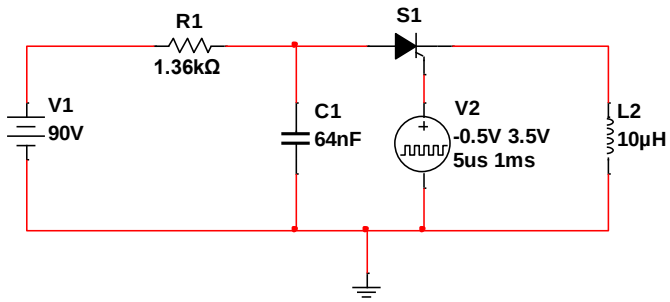

Figure 3.7 Circuit diagram of the Current Pulse Generator Applied from Fig 3.1 Based on Calculation

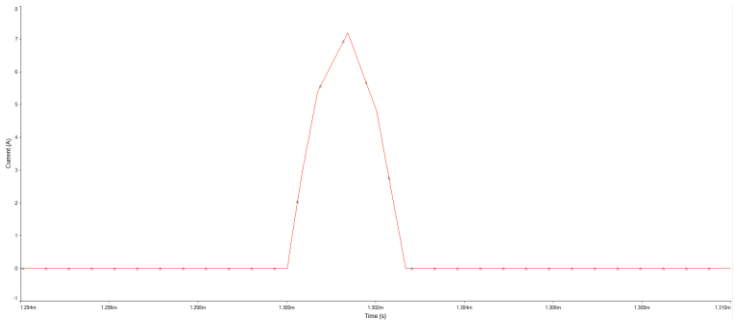

Figure 3.8 Simulation result of Fig 3.7, Coil Current I_{L2}

3.2.2 Combining with Probe & Testing Result

Based on the schematic as is shown in Figure 3.1 and 3.10, the implementation of the circuit is as shown in Figure 3.9. Based on the analysis of the previous section, the final parameters of each component are listed in Table 6.

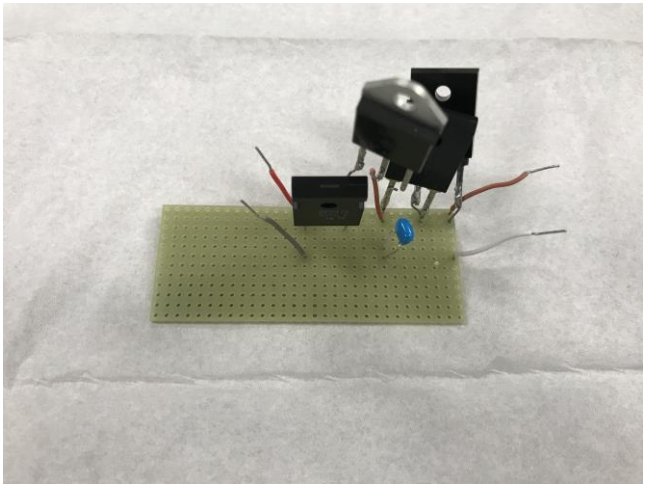

Figure 3.9 A Picture of The Circuit on The Breadboard.

Component	R_1 (Ω)	C_1 (F)	L_2 (H)	SCR
parameter	1360	0.33μ	10 μ	S8035K

Table 6 Parameters of Each Component Used in Fig. 3.9 & 3.10

The final schematic and simulation result of magnetic stimulation circuit is shown as Figure 3.10 – 3.11. Notice that a small 1Ω resistor R_2 is connected to the electromagnetic probe to measure the current of the probe. Based on the simulation result, the magnitude of the current pulse is 14A, and the width of the pulse is 5μs.

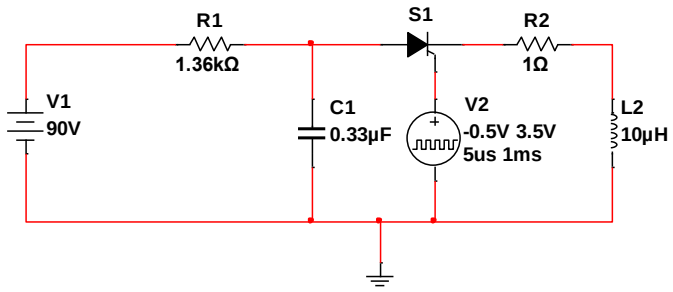

Figure 3.10 Circuit Diagram of Magnetic Stimulation Circuit with Parameters, Adapted from Fig 3.7

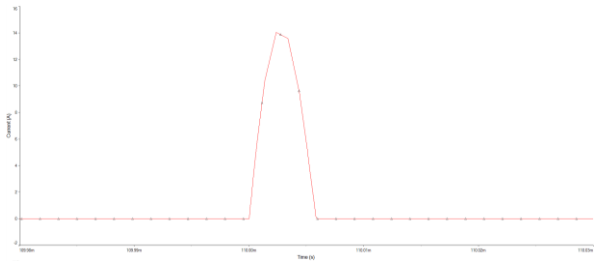

Figure 3.11 Simulation result of Fig 3.10, Coil Current I_{L2}

When V_1 is set to 90V and V_2 is set as Figure 3.12, the overall result for the current pulse and voltage of the detection coil is as shown in Figure 3.13.

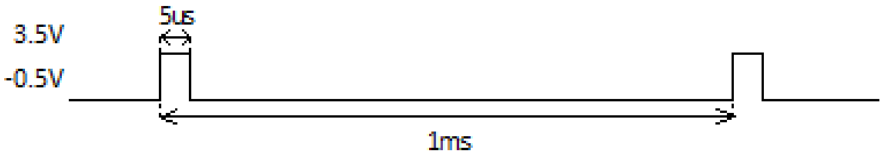

Figure 3.12 Waveform of Function Generator (V_2)

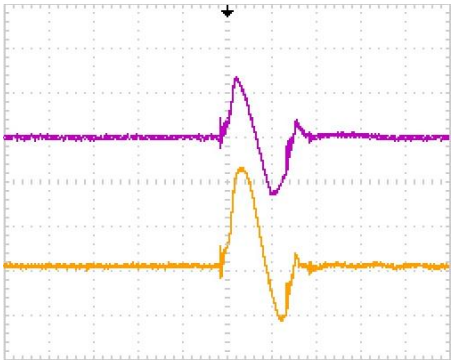

Figure 3.13 Current Pulse (Yellow) and Voltage of The Detection Coil (Purple)

As is shown in Figure 3.14, the scales of the current pulse are 10V and 2.5μs for one grid. Based on the measurement, the magnitude of the current pulse is 44V, which means the current reaches 44A. The width of the pulse is 2.6μs.

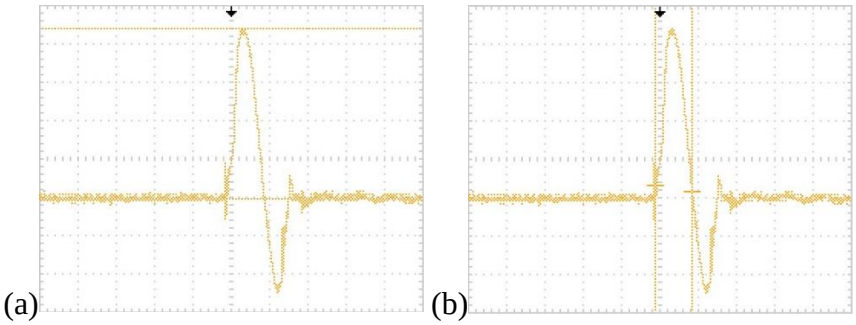

Figure 3.14 (a) Amplitude and (b) Pulse Width of the Coil Current I_{L2}

As is shown in Figure 3.15, the scale of the Detection Coil is 500mV for one grid. Based on the measurement, the voltage of the Detection Coil is 1.34V. Therefore, the induced electric field is as Equation 3.22. This induced electric field meets the requirement of magnetic stimulation.

$$E = \frac{U}{2n(a+b)} = \frac{1.34}{13.6\text{m}} = 98.5\ V/m \tag{3.22}$$

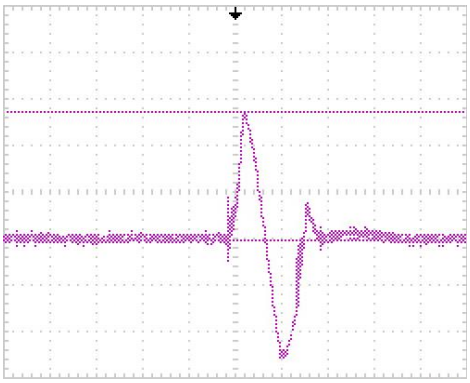

Figure 3.15 Measured (Voltage) Amplitude in The Detection Coil.

The calculation result is not exactly the same as the implementation. The main reason should be the error of measuring the inductance of the probe. Another explanation is that the electrical property of probe is not simply equivalent to an inductor, but rather to other more complicated models. The fluctuations in the function generator (V_2) and DC source (V_1) can also contribute to the error. Based on the experiment data, the actual inductance of the probe should be smaller than 10μH. For Figure 3.10, if L_2 is adjusted to 2μH and the same simulation is performed, the simulation result will be similar to the testing result, as is shown in Figure 3.16.

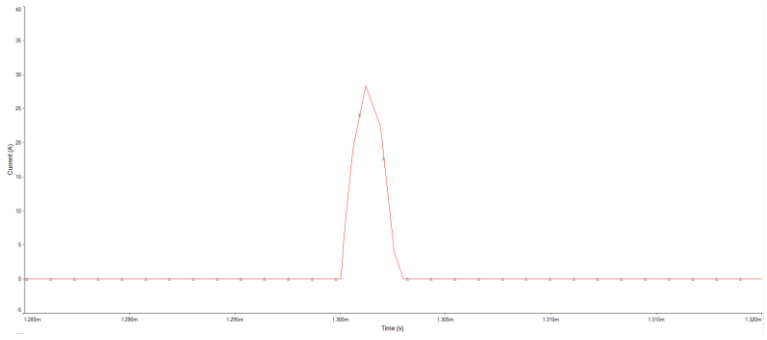

Figure 3.16 Simulation Result of Fig 3.10 with 2μH Inductor L_2, Coil Current I_{L2}

From Figure 3.14 – 3.15, the noise glitch is observed for both the current pulse and the detection coil at the very beginning of the current pulse, the zoom-in view is shown as Figure 3.17 – 3.18.

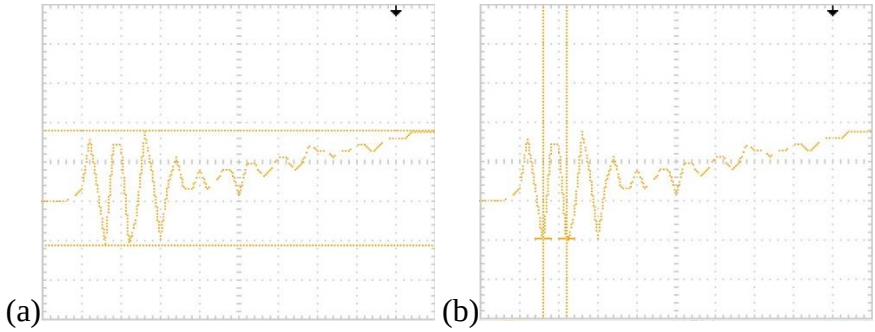

Figure 3.17 (a) Amplitude and (b) Pulse Width of The Current Pulse Noise

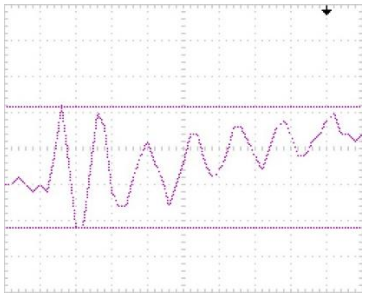

Figure 3.18 Amplitude of the Detection Coil Noise

The glitch is generated from the switching action of SCR, which is called switching noise. The scales of the current pulse noise are 5V and 50ns for one grid. Based on the measurement, the peak-to-peak magnitude of the current pulse noise is 14.4V, which means the magnitude of the noise reaches 7.2A. The period of the noise is around 32ns, which means the frequency of the noise is around 31.25MHz. On the other hand, the scale of Detection Coil Noise is 200mV for one grid. Based on the measurement, the

peak-to-peak voltage of the Detection Coil is 672mV, which means the magnitude of the noise reaches 336mV.

Comparing with the signal, the proportion of the noise is as Equation 3.23 – 3.24.

$$\frac{I_{pulse\_noise}}{I_{pulse}} = \frac{7.2}{44} = 16.4\% \tag{3.23}$$

$$\frac{I_{detector\_noise}}{V_{detector}} = \frac{336\text{m}}{1.34\text{V}} = 25\% \tag{3.24}$$

The effect of noise is not so significant comparing to signal, which is acceptable. It is feasible to apply the appropriate LR filter to finer the waveform, but the magnitude of the current will suffer.

Based on that the noise frequency around 30MHz and the signal frequency is around 200kHz, from Equation 3.11, the relationship between L and R for the filter is shown as Equation 3.25.

$$1.26 \times 10^6 < \frac{R}{L} < 1.89 \times 10^8 \tag{3.25}$$

Taking Equation 3.15 into consideration, if setting R as 20Ω and L as 0.2μH and adding an additional 5A 30MHz current source in parallel with charging part as noise, the schematic and simulation result is as shown in Figure 3.19 – 3.20.

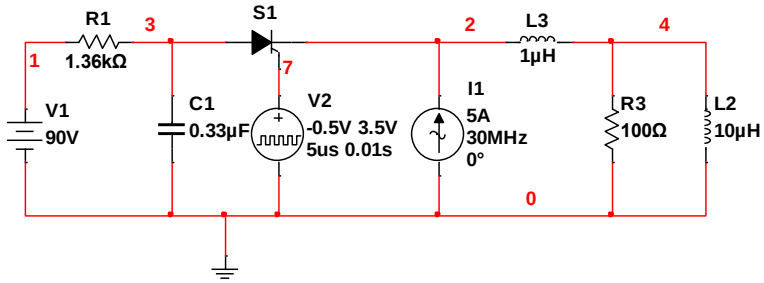

Figure 3.19 Schematic after Applied LR Filter and Current Noise into Fig 3.10

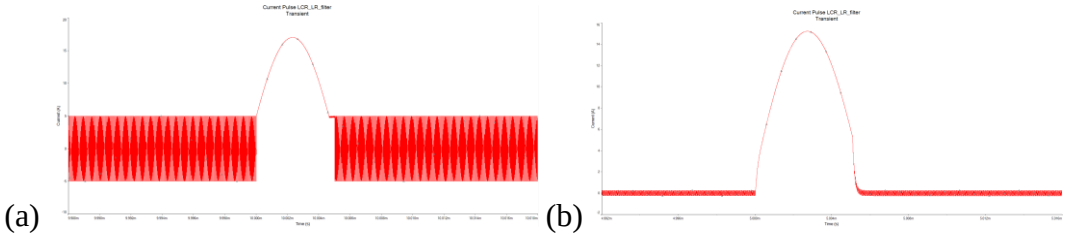

(a) (b)

Figure 3.20 Simulation Result of Fig 3.19, Coil Current I_{L2} (a) Without and (b) With LR Filter

Comparing Figure 3.20(a) with Figure 3.20(b), the high-frequency noise is significantly suppressed, but the magnitude of the current drops from 17.0A to 15.2A, which is the 89.4% of the original one. Therefore, the LR filter is not applied for this implementation.

3.3 Conclusion

The system combining electromagnetic probe and magnetic stimulation circuit is functional and proved to be able to generate the 100 V/m induced electric field on the side of the coil with a 0.5 Amp current pulse in the coil of the probe. The experimental data is not exactly the same as the result of simulation due to several reasons, but it provides a good reference for the implementation.

The LR filter is proved to be functional for suppressing noise based on the simulation with Multisim. However, from the experimental result, the noise does not significantly affect the induced electric field. Taking the attenuation of the current pulse into consideration, the LR filter is not applied for the final implementation.

CHAPTER IV

CONCLUSION AND FUTURE WORK

A miniaturized electromagnetic probe is designed, fabricated and tested to provide focused fields for localized magnetic stimulation. The electromagnetic probe consists of a core with a sharp tip and a surrounding inductive coil. To enhance the field generation, the magnetic core is made of a ferromagnetic alloy with high magnetic permeability and magnetic saturation level.

To optimize the probe design, a detailed finite-element simulation with COMSOL Multiphysics® is performed to study the effect on field generation by a few key factors, including material composition, magnetic properties, core shape and size, number of turns of the coil, etc. It is discovered that the induced electric field near the side of the core is higher than near the tip.

For experimental validation, a prototype electromagnetic probe is fabricated and connected to the developed magnetic stimulation circuit. A home-made pick-up coil is used to measure the induced electric field at the side of the core. The result shows that the system is able to generate the desired electric field.

Another electromagnetic coil is designed and tested to provide even distributed intensity of the induced electric field for a larger area of magnetic stimulation. The electromagnetic coil is wired in a cylindrical shape, and a cylindrical-annulus-shaped core could be applied to enhance the magnetic flux density. To optimize the right structure for larger area magnetic stimulation, finite-element simulation with COMSOL

Multiphysics® is performed for a cylindrical-shaped coil structure. The key factors studied include size, number of turns, weight, and heat generation, etc.

A magnetic stimulation circuit for the small probe is designed, fabricated and tested. The main performance specs of the stimulation circuit are pulse width, amplitude, duration and pulse repetition rate, etc. This circuit is designed to operate in two cycles: charging and discharging cycles. The pulse width and amplitude are related to several parameters including capacitance/inductance, operation voltage, etc. The duration and repetition rate are controlled by the frequency and the duty ratio of the pulse generator, which switches the circuit between these two cycles, and thus control the duration and repetition rate.

To optimize the circuit design, a detailed simulation with Multisim® is conducted to determine the relationship between the profile of the output current pulses and key circuit parameters, including operation voltage, capacitance, inductance, frequency, the duty ratio, etc. Combining with the result of the simulation, circuit parameters are optimized to meet the performance requirement. For experimental verification, a prototype stimulation circuit is fabricated and tested. The testing results show that it is able to provide a desired current pulse for the probe and coil.

This study demonstrates the feasibility of micromagnetic stimulation system for magnetic stimulation of small animal brains in ex-vivo condition. In the future, in-vivo applications of the micromagnetic stimulation system on small animal brains will be explored.

REFERENCES

[1] Yamaguchi, S., M. Ogiue-Ikeda, M. Sekino, and S. Ueno. "Effects of magnetic stimulation on tumors and immune functions." IEEE transactions on magnetics 41, no. 10 (2005): 4182-4184.

[2] Mohri, Kaneo, Tsuyoshi Uchiyama, Muneo Yamada, Yoshiyuki Mohri, K. Endo, T. Suzuki, and Yasuya Inden. "Physiological magnetic stimulation for arousal of elderly car driver evaluated with electro-encephalogram and spine magnetic field." IEEE Transactions on Magnetics 48, no. 11 (2012): 3505-3508.

[3] Chang, Yu, Miao Song, Bin Gao, Ningning Chen, Ling Li, and Hongxing Wang. "Magnetic Field Distribution and Application of a Transcranial Magnetic Stimulation for Drug Addicts." In 2009 3rd International Conference on Bioinformatics and Biomedical Engineering, pp. 1-4. IEEE, 2009.

[4] Shu, Xiaokang, Shugeng Chen, Guohong Chai, Xinjun Sheng, Jie Jia, and Xiangyang Zhu. "Neural Modulation By Repetitive Transcranial Magnetic Stimulation (rTMS) for BCI Enhancement in Stroke Patients." In 2018 40th Annual International Conference of the IEEE Engineering in Medicine and Biology Society (EMBC), pp. 2272-2275. IEEE, 2018.

[5] Roth, Bradley J., and Peter J. Basser. "A model of the stimulation of a nerve fiber by electromagnetic induction." IEEE Transactions on Biomedical Engineering 37, no. 6 (1990): 588-597.

[6] RamRakhyani, Anil Kumar, Zachary B. Kagan, David J. Warren, Richard A. Normann, and Gianluca Lazzi. "A μm-Scale Computational Model of Magnetic Neural Stimulation in Multifascicular Peripheral Nerves." IEEE Transactions On Biomedical Engineering 62, no. 12 (2015): 2837-2849.

[7] Basser, Peter J., Ranjith S. Wijesinghe, and Bradley J. Roth. "The activating function for magnetic stimulation derived from a three-dimensional volume conductor model." IEEE transactions on biomedical engineering 39, no. 11 (1992): 1207-1210.

[8] Åström, Mattias, Elin Diczfalusy, Hubert Martens, and Karin Wårdell. "Relationship between neural activation and electric field distribution during deep brain stimulation." IEEE Transactions on Biomedical Engineering 62, no. 2 (2015): 664-672.

[9] Peterchev, Angel V., Timothy A. Wagner, Pedro C. Miranda, Michael A. Nitsche, Walter Paulus, Sarah H. Lisanby, Alvaro Pascual-Leone, and Marom Bikson. "Fundamentals of transcranial electric and magnetic stimulation dose: definition, selection, and reporting practices." Brain stimulation 5, no. 4 (2012): 435-453.

[10] Makowski, Nathaniel S., Jayme S. Knutson, John Chae, and Patrick Crago. "Neuromuscular electrical stimulation to augment reach and hand opening after stroke." In 2011 Annual International Conference of the IEEE Engineering in Medicine and Biology Society, pp. 3055-3058. IEEE, 2011.

[11] Salimpour, Yousef, Chang-Chia Liu, William R. Webber, Kelly A. Mills, and William S. Anderson. "Subdural recordings from an awake human brain for measuring current intensity during transcranial direct current stimulation." In 2017 39th Annual International Conference of the IEEE Engineering in Medicine and Biology Society (EMBC), pp. 1110-1113. IEEE, 2017.

[12] Sharma, Gaurav, Yashika Arora, and Shubhajit Roy Chowdhury. "A 4X1 high-definition transcranial direct current stimulation device for targeting cerebral micro vessels and functionality using NIRS." In 2016 IEEE International Symposium on Nanoelectronic and Information Systems (iNIS), pp. 47-51. IEEE, 2016.

[13] Zhang, Liyan, Zuhe Wu, Xianwen Zhang, and Jintian Tang. "Performance in Motor Imagery Tasks can be improved by Transcranial Alternating Current Stimulation." In 2016 9th International Congress on Image and Signal Processing, BioMedical Engineering and Informatics (CISP-BMEI), pp. 1707-1711. IEEE, 2016.

[14] Terney, Daniella, Leila Chaieb, Vera Moliadze, Andrea Antal, and Walter Paulus. "Increasing human brain excitability by transcranial high-frequency random noise stimulation." Journal of Neuroscience 28, no. 52 (2008): 14147-14155.

[15] Wu, Zuhe, JinJin Liu, and Jun Ma. "A novel cranial electrotherapy stimulation system with arbitrary waveform stimulation." In 2014 7th International Conference on Biomedical Engineering and Informatics, pp. 517-521. IEEE, 2014.

[16] Deng, Zhi-De, Sarah H. Lisanby, and Angel V. Peterchev. "Effect of anatomical variability on electric field characteristics of electroconvulsive therapy and magnetic seizure therapy: a parametric modeling study." IEEE Transactions on Neural Systems and Rehabilitation Engineering 23, no. 1 (2015): 22-31.

[17] Deng, Zhi-De, Sarah H. Lisanby, and Angel V. Peterchev. "Effect of anatomical variability on neural stimulation strength and focality in electroconvulsive therapy (ECT) and magnetic seizure therapy (MST)." In 2009 Annual International Conference of the IEEE Engineering in Medicine and Biology Society, pp. 682-688. IEEE, 2009.

[18] Khairunnahar, Laila, Md Kamal Hosain, and Md Rabiul Islam. "Determination of EM parameters in human head phantom by transcranial magnetic stimulation." In 2017 3rd International Conference on Electrical Information and Communication Technology (EICT), pp. 1-6. IEEE, 2017.

[19] Nakamura, Yusaku, Hikaru Sakamoto, Ikuko Yamada, and Kazuto Hirano. "Suppressive effect on focal upper extremity dystonia after repetitive 1Hz transcranial magnetic stimulation." In The 2011 IEEE/ICME International Conference on Complex Medical Engineering, pp. 145-147. IEEE, 2011.

[20] Deng, Zhi-De, and Sarah H. Lisanby. "Electric field characteristics of low-field synchronized transcranial magnetic stimulation (sTMS)." In 2017 39th Annual International Conference of the IEEE Engineering in Medicine and Biology Society (EMBC), pp. 1445-1448. IEEE, 2017.

[21] Hasan, Md Mahmudul, Shahed Md Abu Sufian, Hasan Mehdi, and Khondkar Siddique-e-Rabbani. "Designing a transcranial magnetic stimulator coil for deep brain stimulation." In 2016 9th International Conference on Electrical and Computer Engineering (ICECE), pp. 303-306. IEEE, 2016.

[22] Vegas, Jefferson and Alexander Misdorp. "Focal coil design for transcranial magnetic stimulation on mice." Bachelor Thesis, Delft University of Technology, 2016. http://resolver.tudelft.nl/uuid:1def5977-19eb-45f2-90ba-52374bd7565e

[23] Gabran, S. R. I., J. H. Saad, M. M. A. Salama, and R. R. Mansour. "Finite difference time domain (FDTD) modeling of implanted deep brain stimulation electrodes and brain tissue." In 2009 Annual International Conference of the IEEE Engineering in Medicine and Biology Society, pp. 6485-6488. IEEE, 2009.

[24] Peterchev, Angel V., Reza Jalinous, and Sarah H. Lisanby. "A transcranial magnetic stimulator inducing near-rectangular pulses with controllable pulse width (cTMS)." IEEE Transactions on Biomedical Engineering 55, no. 1 (2008): 257-266.

[25] Goetz, Stefan M., Bruce Luber, Sarah H. Lisanby, David LK Murphy, I. Cassie Kozyrkov, Warren M. Grill, and Angel V. Peterchev. "Enhancement of neuromodulation with novel pulse shapes generated by controllable pulse parameter transcranial magnetic stimulation." Brain stimulation 9, no. 1 (2016): 39-47.

[26] Peterchev, Angel V. "Circuit topology comparison and design analysis for controllable pulse parameter transcranial magnetic stimulators." In 2011 5th International IEEE/EMBS Conference on Neural Engineering, pp. 646-649. IEEE, 2011.

[27] Peterchev, Angel V., and David L. Murphy. "Controllable pulse parameter transcranial magnetic stimulator with enhanced pulse shaping." In 2013 6th International IEEE/EMBS Conference on Neural Engineering (NER), pp. 121-124. IEEE, 2013.

[28] Barnes, Walter L., Won Hee Lee, and Angel V. Peterchev. "Approximating transcranial magnetic stimulation with electric stimulation in mouse: a simulation study." In 2014 36th Annual International Conference of the IEEE Engineering in

Medicine and Biology Society, pp. 6129-6132. IEEE, 2014.

[29] Rastogi, P., R. L. Hadimani, and D. C. Jiles. "Investigation of coil designs for transcranial magnetic stimulation on mice." IEEE Transactions on Magnetics 52, no. 7 (2016): 1-4.

[30] Selvaraj, Jayaprakash, Priyam Rastogi, Neelam Prabhu Gaunkar, Ravi L. Hadimani, and Mani Mina. "Transcranial Magnetic Stimulation: Design of a stimulator and a focused coil for the application of small animals." IEEE Transactions on Magnetics 99 (2018): 1-5.

[31] Peterchev, Angel V., Sameer C. Dhamne, Raveena Kothare, and Alexander Rotenberg. "Transcranial magnetic stimulation induces current pulses in transcranial direct current stimulation electrodes." In 2012 Annual International Conference of the IEEE Engineering in Medicine and Biology Society, pp. 811-814. IEEE, 2012.

[32] Salvador, Ricardo, and P. C. Miranda. "Transcranial magnetic stimulation of small animals: a modeling study of the influence of coil geometry, size and orientation." In 2009 annual international conference of the IEEE engineering in medicine and biology society, pp. 674-677. IEEE, 2009.

[33] Bonmassar, G. "Advancing coil design in micromagnetic brain stimulation." In 2017 International Conference on Electromagnetics in Advanced Applications (ICEAA), pp. 1875-1878. IEEE, 2017.

[34] Shin, Jong Yoon, Jae-Hyun Ahn, Kilhwa Pi, Dong-il Dan Cho, and Yong Sook Goo. "Electrodeless, non-invasive stimulation of retinal neurons using time-varying magnetic fields." In 2015 IEEE SENSORS, pp. 1-4. IEEE, 2015.

[35] Lee, Seung Woo, and Shelley I. Fried. "Magnetic stimulation of subthalamic nucleus neurons using micro-coils for deep brain stimulation." In 2013 6th International IEEE/EMBS Conference on Neural Engineering (NER), pp. 133-135. IEEE, 2013.

[36] Lee, Seung Woo, and Shelley I. Fried. "Suppression of subthalamic nucleus activity by micromagnetic stimulation." IEEE Transactions on Neural Systems and Rehabilitation Engineering 23, no. 1 (2015): 116-127.

[37] Lee, Seung Woo, and Shelley I. Fried. "The response of L5 pyramidal neurons of the PFC to magnetic stimulation from a micro-coil." In 2014 36th Annual International Conference of the IEEE Engineering in Medicine and Biology Society, pp. 6125-6128. IEEE, 2014.

[38] Huang, Ying-Zu, Martin Sommer, Gary Thickbroom, Masashi Hamada, Alvero Pascual-Leonne, Walter Paulus, Joseph Classen, Angel V. Peterchev, Abraham Zangen,

and Yoshikazu Ugawa. "Consensus: New methodologies for brain stimulation." Brain stimulation 2, no. 1 (2009): 2-13.

[39] Yapici, Murat Kaya, and Jun Zou. "Permalloy-coated tungsten probe for magnetic manipulation of micro droplets." Microsystem Technologies 14, no. 6 (2008): 881-891.

[40] Shoihet, Arthur, Moshe Shvartsas, Beni Gdaliahu, and Itzik Edry. "High current short pulse generator for pulse magneto-oscillation (PMO) research." In 2012 IEEE 27th Convention of Electrical and Electronics Engineers in Israel, pp. 1-5. IEEE, 2012.